Seventh International Conference on Computational Fluid Dynamics (ICCFD7), Big Island, Hawaii, July 9-13, 2012 **ICCFD7-3804**

Dynamic Mesh Deformation for Implicit Adaptive Non-Linear Frequency Domain Method

Ali Mosahebi* and Siva Nadarajah*
Corresponding author: ali.mosahebimohamadi@mail.mcgill.ca

*McGill University, CFD Lab, Department of Mechanical Engineering, Montreal, Quebec, Canada.

Abstract: An innovative implicit adaptive Nonlinear Frequency Domain method (adaptive NLFD) has been implemented for the Navier-Stokes equations on deformable grids. For periodic flow problems, not only a spectral temporal accuracy could be achieved via transformation of the governing equations to the frequency domain, but a large reduction in the computational costs is realized when compared to a classical time marching approach. In the present study, the computational efficiency is even further enhanced through the implementation of the adaptive NLFD concept. For numerical simulation of general periodic problems, the concept of dynamic or moving/deformable grid is implemented. To accelerate the convergence rate, a modified nonlinear LU-SGS technique is proposed. Results are presented for the laminar vortex shedding behind a stationary 2D cylinder, a plunging, and a pitching airfoil and are compared with previous numerical results as well as experimental data.

Keywords: Periodic Flow, Adaptive NLFD Method, Non-Linear LU-SGS Method, Deformable Grid, Vortex Shedding, Stationary Cylinder, Plunging Airfoil, Pitching Airfoil.

1 Introduction

Despite great improvements in the numerical simulation of steady state fluid flow problems, developing fast and accurate approaches for the simulation of unsteady problems continues to pose a severe challenge in Computational Fluid Dynamics (CFD). To obtain a reliable unsteady solution, temporal evolution of the flow should be accurately resolved, while preserving precise spatial discretizations. Unsteady problems can be categorized in two major groups; (i) flows that show repeating patterns over a specific time interval, time period (T), and (ii) flows that are inherently unsteady having no special pattern over time. In the present study, the flows belonging to the first group which are usually named as periodic flows are investigated. Periodic phenomena widely appear in industrial as well as natural problems. For instance, fluid flow around helicopter rotor blades and wind turbines, and through the compressor and turbine stages of turbomachinary devices are some of well-known industrial applications of periodic flows. Vortex shedding behind bluff bodies and other similar cases showing instabilities within free shear layers are some of the natural examples of periodic flows.

Traditional time marching schemes require a large number of time steps for the initial transient solutions to diminish before a periodic solution is obtained, requiring vast computational resources. In problems where the frequency is generally known, such as the blade passing frequency in turbomachinery or the revolutions per minute of helicopter blades, the development of schemes that exploit this key condition have been progressing for the past several decades starting with the linearized frequency domain technique [1–6], followed by the deterministic stress method [7–9].

Hall *et* al. [10, 11] introduced the Harmonic Balance approach, a fully non-linear technique, that considers the complete nonlinearities of the governing equations. The method was further validated by McMullen *et* al. [13–16]. These methods are based on transforming the governing equations from the physical or time domain to the frequency domain. McMullen *et* al. [13, 14] solved these equations in the frequency domain, while Hall *et* al [10] transformed them back to the time domain. Regardless of selecting the frequency or the time domain for the pseudo iterative marching of the equations, both methods are conceptually similar. When the equations are transformed back to the physical domain, the time derivative appears to be discretized as a high-order central difference term coupling all the time levels in the period. Therefore, these methods are usually known as time spectral methods.

Although the NLFD method provides a great improvement in execution time, it requires relatively large amounts of computational memory which restricts its computational efficiency. Reducing this large memory demand not only solves the memory restriction, but also increases the computational speed. In majority of periodic flows, highly unsteady flow regions are typically restricted to the wake of an object in external flow, such as the separated regions of the trailing edge, the tip regions of an aerodynamic surface, as well as in the vicinity of a moving shock wave. In these regions the fluid varies at frequencies that are multiples of the fundamental frequency. Hence one can conjecture that the number of these higher frequencies or modes are localized in specific regions of the flow, while leaving other regions the ability to be resolved with a lower frequency content. This concept was intially proposed by Maple *et* al. [18] for a quasi-one-dimensional Euler flow. Extension of the adaptive concept to 2D viscous flows was performed by the present authors [19].

For the NLFD method, the time marching is in pseudo rather than real time; therefore, various convergence accelerators may be used to enhance the convergence rate. Most importantly, in this study, a nonlinear LU-SGS technique is modified and employed to replace conventional explicit time marching approaches. Since, the temporal accuracy of the results in the NLFD method is not a function of the time step, but the number of modes, mathematically, this implicit approach provides the same accurate results as the explicit methods. In the frequency domain, this method was first employed by Cagnone and Nadarajah [20] for the Euler equations. Later, it was extended to the viscous flows by the present authors [21]. In this study, the method is modified by coupling the mode equations to enhance its computational efficiency and robustness.

Finally, the deformable grid concept, which was perviously employed for the adaptive NLFD method by the present authors [21], is extended to the developed implicit solver. Having a deformable grid is a need for more realistic periodic problems, where the rigid grid movements cannot properly handle the object movements. In this study, the laminar vortex shedding behind a 2D stationary cylinder, a plunging, and a pitching airfoil is investigated and compared with previous numerical and experimental results.

2 Governing Equations and their Discretization

For viscous flows the unsteady Navier-Stokes equations in the integral form are as follow,

$$\frac{\partial}{\partial t}\int_{\Omega}\vec{w}d\Omega + \oint_{\partial\Omega}(\vec{F}_c - \vec{F}_v)dS = 0, \tag{1}$$

where Ω is a control volume, $\partial\Omega$ is the volume boundary with dS as its surface element, $\vec{w}$ is the state vector, and $\vec{F}_c$ and $\vec{F}_v$ are inviscid and viscous flux vectors, respectively. These vectors are defined in a general ALE form as follows,

$$\vec{w} = \left\{\begin{array}{c}\rho\\ \rho u\\ \rho v\\ \rho E\end{array}\right\},\ \vec{F}_c = \left\{\begin{array}{c}\rho V_r\\ \rho u V_r + n_x p\\ \rho v V_r + n_y p\\ \rho H V_r + p V_t\end{array}\right\},\ \text{and } \vec{F}_v = \left\{\begin{array}{c}0\\ n_x\tau_{xx} + n_y\tau_{xy}\\ n_x\tau_{yx} + n_y\tau_{yy}\\ n_x\theta_x + n_y\theta_y\end{array}\right\}, \tag{2}$$

where,

$$\theta_x = u\tau_{xx} + v\tau_{xy} + k\frac{\partial T}{\partial x},\ \text{and } \theta_y = u\tau_{yx} + v\tau_{yy} + k\frac{\partial T}{\partial y}. \tag{3}$$

In these equations, $\rho, u, v, T, E,\ H,$ and p denote the density, the cartesian velocity components, the temperature, the total energy per unit mass, the total or stagnation enthalpy, and the pressure respectively, where the pressure is evaluated through the equation of state for ideal gases. Besides, n_x and n_y are the components of the outward facing unit normal vector of the surface $\partial\Omega$. $V = n_x u + n_y v$, $V_r = V - V_t$,and $V_t = n_x \dfrac{\partial x}{\partial t} + n_y \dfrac{\partial y}{\partial t}$ are the flow velocity vector, contravariant flow velocity relative to the motion of the grid, and the contravariant velocity of the face of the control volume. Newtonian viscous behavior is considered for the viscous stresses. The non-dimensionalized form of Eq (1) for a discretized control volume could be obtained as follows,

$$\frac{\partial(\Omega\vec{w})}{\partial t} + \sum_{\partial\Omega}(\vec{F}_c - \vec{F}_d)S - \frac{\sqrt{\gamma}M_\infty}{Re_\infty}\sum_{\partial\Omega}\vec{F}_v S = 0, \tag{4}$$

where, the artificial dissipation vector $\vec{F}_d$, based on the Roe method [22], is added to the convective flux vector to ensure stability. To produce a system of coupled Ordinary Differential Equations (ODE) and advancing this system forward in time, the following semi-discrete form of the equations is considered,

$$\frac{d(\Omega w)}{dt} + R(w) = 0, \tag{5}$$

where the residual, $R(w)$, is evaluated by summing the fluxes through the cell faces. Therefore, different spatial and temporal discretization techniques may be used for the numerical modelling of the residual and temporal evolution of the state vector, respectively.

2.1 Spatial Discretization

A second-order spatial discretization accuracy for the convective fluxes is achieved through using the Roe flux splitting approach [22] combined with a second-order MUSCL technique ($\kappa = \dfrac{1}{3}$ and $\epsilon = 1$) [23]. Viscous fluxes are constructed using the same accurate finite volume discretization techniques [24].
Equation (5) can then be written for each computational cell as,

$$\frac{d(\Omega_{i,j} w_{i,j})}{dt} + R(w)_{i,j} = 0, \tag{6}$$

where $R(w)_{i,j}$ represents the summation of all fluxes across the control volume (i,j) faces.

2.2 Temporal Discretization

The main assumption in the NLFD method is that for a periodic flow, the Fourier series can be employed to represent periodic temporal behavior of the flow characteristics. Considering Eq. (6), the modified state $(\bar{w} = \Omega w)$ and residual vectors at each control volume (i,j) can be expressed as,

$$\begin{gathered}
\bar{w}(t) = a_0 + \sum_{k=1}^{m} a_k \cos(\frac{2\pi k}{T}t) + \sum_{k=1}^{m} b_k \sin(\frac{2\pi k}{T}t), \\
R(t) = a'_0 + \sum_{k=1}^{m} a'_k \cos(\frac{2\pi k}{T}t) + \sum_{k=1}^{m} b'_k \sin(\frac{2\pi k}{T}t), \\
\text{or} \\
\bar{w}(t) = \sum_{k=-m}^{m} \hat{w}_k e^{i\frac{2\pi k}{T}t}, \qquad R(t) = \sum_{k=-m}^{m} \hat{R}_k e^{i\frac{2\pi k}{T}t}.
\end{gathered} \tag{7}$$

In these equations, T is the time period, $i = \sqrt{-1}$, k is the wave number, a_k, b_k, a'_k, and b'_k are coefficients denoting amplitudes of the sine and cosine waves of the modified state and residual vectors, respectively.

Similarly, $\hat{w}_k$ and $\hat{R}_k$ are the Fourier representations of these flow variables in the complex domain. Thanks to the fact that the solution of real physical problems do not have any imaginary parts, the Fourier coefficients for the negative wave numbers are simply the complex conjugates of the coefficients for the positive wave numbers and can be eliminated in the computational procedure. As a result, the complex coefficients in these Fourier representations can be related to the real ones, *e.g.* for $\hat{w}_k$,

$$\begin{cases} \hat{w}_k = \frac{a_k}{2} - \frac{b_k}{2}i & k > 0 \\ \hat{w}_0 = a_0 & k = 0 \\ \hat{w}_{-|k|} = \bar{\hat{w}}_{|k|} = \frac{a_{|k|}}{2} + \frac{b_{|k|}}{2}i & k < 0. \end{cases} \tag{8}$$

The Fourier representations in Eq. (7) are then substituted into the semi-discretized form of the governing equations as described in Eq. (6) to yield,

$$\frac{d}{dt}\left[\sum_{k=-m}^{m} \hat{w}_k e^{i\frac{2\pi k}{T}t}\right] + \sum_{k=-m}^{m} \hat{R}_k e^{i\frac{2\pi k}{T}t} = 0 \qquad \text{in } \Omega. \tag{9}$$

Thanks to the orthogonality of the Fourier base functions, a separate equation for each wave number is resulted,

$$\hat{R}_k^* = \frac{2\pi k}{T}\hat{w}_k i + \hat{R}_k = 0 \qquad \text{in } \Omega \text{ for } 0 \leq k \leq m. \tag{10}$$

Since within a cell, $\hat{R}_k$ is a nonlinear function of $\hat{w}_\gamma$ $(0 \leq \gamma \leq m)$ of the cell and its neighbors, a pseudo time marching approach should be employed to solve the system of equations iteratively,

$$\frac{d\hat{w}_k}{dt^*} + \hat{R}_k^* = 0. \tag{11}$$

When convergence is achieved, $\frac{d\hat{w}_k}{dt^*} = 0$, the desired results for Eq. (10) would be obtained. In the frequency domain, $\hat{w}$ and $\hat{R}$ is evaluated respectively through the transformations of $\bar{w}(t)$ and $R(t)$ from the time domain via FFTs. Therefore, for computation of the residual within the time domain, any conventional spatial discreitzation technique, *e.g.* Roe method, may be used. Within the frequency domain, $\hat{w}_k$ is updated using Eq. (11). To complete the loop, an inverse FFT is then used to transform back $\hat{w}_k$ to the time domain which results in the new updated modified state vector, $\bar{w}(t)$, sampled at evenly distributed intervals over the time period. The state vector can be easily obtained from $w(t) = \frac{\bar{w}(t)}{\Omega(t)}$. Boundary conditions are updated within the time domain, where for the wall, a no slip boundary condition and for the farfield the characteristic boundary conditions are imposed.

It should be mentioned that for the NLFD method, the grid movement is represented through a similar Fourier expression as the state vector. Therefore, the so called Geometric Conservation Law for the grid velocity evaluation could be easily satisfied. For instance, for the x velocity component,

$$x(t) = \sum_{k=-m}^{m} \hat{x}_k e^{\frac{2\pi k i}{T}t} \Rightarrow x^{\cdot}(t) = \sum_{k=-m}^{m} \hat{x}_k \frac{2\pi k i}{T} e^{\frac{2\pi k i}{T}t} \tag{12}$$

Substituting Eq. (8) into Eq. (11) and using a first-order backward Euler method for the implicit temporal discretization results into the following coupled system of equations for updating the, a_k and b_k, coefficients,

$$\begin{aligned} &\frac{a_k^{n+1} - a_k^n}{\Delta t^*} + a'^{n+1}_k + \frac{2\pi k}{T} b_k^{n+1} = 0 \quad \forall \quad 0 \leq k \leq m, \\ &\frac{b_k^{n+1} - b_k^n}{\Delta t^*} + b'^{n+1}_k - \frac{2\pi k}{T} a_k^{n+1} = 0 \quad \forall \quad 1 \leq k \leq m. \end{aligned} \tag{13}$$

Since the same numerical approach is employed for these two sets of equations (for a_k and b_k coefficients) throughout the paper; only discretization of the first equation (a_k coefficients) is explained. It is clear that a similar approach may be used for the second equation (b_k coefficients). Difficulties in solving the above system of equations comes from the fact that the residual coefficients, ${a'}_k^{n+1}$ and ${b'}_{k,}^{n+1}$ are nonlinear functions of the state coefficients, a_γ^{n+1} and b_γ^{n+1}, for all of wave numbers ($0 \leq \gamma \leq m$) of the control volume and its neighbors. However, these coefficients could be related together through a Newton-Raphson linearization.

$$\begin{aligned} {a'}_k^{n+1} &= {a'}_k^n + \sum_{\gamma=0}^{m} \frac{\partial a'_k}{\partial a_\gamma}(a_\gamma^{n+1} - a_\gamma^n) + \sum_{\gamma=1}^{m} \frac{\partial a'_k}{\partial b_\gamma}(b_\gamma^{n+1} - b_\gamma^n) \\ &+ \sum_{nb}\sum_{\gamma=0}^{m} \frac{\partial a'_k}{\partial a_{\gamma,nb}}(a_{\gamma,nb}^{n+1} - a_{\gamma,nb}^n) + \sum_{nb}\sum_{\gamma=1}^{m} \frac{\partial a'_k}{\partial b_{\gamma,nb}}(b_{\gamma,nb}^{n+1} - b_{\gamma,nb}^n), \end{aligned} \tag{14}$$

where, nb signifies neighboring control volumes. Substituting these expressions into the system of equations (13) results into,

$$\begin{aligned} &\frac{a_k^{n+1} - a_k^n}{\Delta t^*} + \frac{2\pi k}{T} b_k^{n+1} + {a'}_k^n + \sum_{\gamma=0}^{m} \frac{\partial a'_k}{\partial a_\gamma}(a_\gamma^{n+1} - a_\gamma^n) + \sum_{\gamma=1}^{m} \frac{\partial a'_k}{\partial b_\gamma}(b_\gamma^{n+1} - b_\gamma^n) \\ &+ \sum_{nb}\sum_{\gamma=0}^{m} \frac{\partial a'_k}{\partial a_{\gamma,nb}}(a_{\gamma,nb}^{n+1} - a_{\gamma,nb}^n) + \sum_{nb}\sum_{\gamma=1}^{m} \frac{\partial a'_k}{\partial b_{\gamma,nb}}(b_{\gamma,nb}^{n+1} - b_{\gamma,nb}^n) = 0 \qquad \forall \quad 0 \leq k \leq m. \end{aligned} \tag{15}$$

Direct solution of the above equation is computationally expensive due to the contribution of the neighboring cells. Alternatively, a Gauss-Seidel approach which allows transferring of the neighbors' contribution to the Righ-Hand-Side (RHS) and then solves the above system of equations iteratively, is employed. In this approach, within each sub-iteration, the contributions of the neighbors are calculated using the latest available update of the unknowns which are presented with superscript $(n+1, s)$ and the unknowns at $(n+1, s+1)$ are obtained,

$$\begin{aligned} &\frac{a_k^{n+1,s+1} - a_k^n}{\Delta t^*} + \frac{2\pi k}{T} b_k^{n+1,s+1} + \sum_{\gamma=0}^{m} \frac{\partial a'_k}{\partial a_\gamma}(a_\gamma^{n+1,s+1} - a_\gamma^n) + \sum_{\gamma=1}^{m} \frac{\partial a'_k}{\partial b_\gamma}(b_\gamma^{n+1,s+1} - b_\gamma^n) \\ &= -\left\{ {a'}_k^n + \sum_{nb}\sum_{\gamma=0}^{m} \frac{\partial a'_k}{\partial a_{\gamma,nb}}(a_{\gamma,nb}^{n+1,s} - a_{\gamma,nb}^n) + \sum_{nb}\sum_{\gamma=1}^{m} \frac{\partial a'_k}{\partial b_{\gamma,nb}}(b_{\gamma,nb}^{n+1,s} - b_{\gamma,nb}^n) \right\} \qquad \forall \quad 0 \leq k \leq m. \end{aligned} \tag{16}$$

The scheme is still computationally expensive since the neighbors' Jacobians should be computed and stored on the RHS. The direct contribution of the neighbors could be replayed by an extra cost of re-evaluation of the residual within each sub-iteration s as follows,

$$\begin{aligned} &\underbrace{a'_k(a_\gamma^n, b_\gamma^n, a_{\gamma,nb}^n, b_{\gamma,nb}^n)}_{{a'}_k^n} + \sum_{nb}\sum_{\gamma=0}^{m} \frac{\partial a'_k}{\partial a_{\gamma,nb}}(a_{\gamma,nb}^{n+1,s} - a_{\gamma,nb}^n) + \sum_{nb}\sum_{\gamma=1}^{m} \frac{\partial a'_k}{\partial b_{\gamma,nb}}(b_{\gamma,nb}^{n+1,s} - b_{\gamma,nb}^n) \\ &\qquad\qquad\qquad\qquad \approx a'_k(a_\gamma^n, b_\gamma^n, a_{\gamma,nb}^{n+1,s}, b_{\gamma,nb}^{n+1,s}) \\ &\approx \underbrace{a'_k(a_\gamma^{n+1,s}, b_\gamma^{n+1,s}, a_{\gamma,nb}^{n+1,s}, b_{\gamma,nb}^{n+1,s})}_{{a'}_k^{n+1,s}} - \sum_{\gamma=0}^{m} \frac{\partial a'_k}{\partial a_\gamma}(a_\gamma^{n+1,s} - a_\gamma^n) - \sum_{\gamma=1}^{m} \frac{\partial a'_k}{\partial b_\gamma}(b_\gamma^{n+1,s} - b_\gamma^n), \end{aligned} \tag{17}$$

where, γ in the arguments is $0 \leq \gamma \leq m$ for a_γ and $1 \leq \gamma \leq m$ for b_γ coefficients. Using this approximation results into the following formula for updating the unknowns at each sub-iteration,

$$\begin{aligned} &\frac{a_k^{n+1,s+1} - a_k^n}{\Delta t^*} + \frac{2\pi k}{T} b_k^{n+1,s+1} + \sum_{\gamma=0}^{m} \frac{\partial a'_k}{\partial a_\gamma}(a_\gamma^{n+1,s+1} - a_\gamma^n) + \sum_{\gamma=1}^{m} \frac{\partial a'_k}{\partial b_\gamma}(b_\gamma^{n+1,s+1} - b_\gamma^n) \\ &= -\left\{ {a'}_k^{n+1,s} - \sum_{\gamma=0}^{m} \frac{\partial a'_k}{\partial a_\gamma}(a_\gamma^{n+1,s} - a_\gamma^n) - \sum_{\gamma=1}^{m} \frac{\partial a'_k}{\partial b_\gamma}(b_\gamma^{n+1,s} - b_\gamma^n) \right\} \qquad \forall \quad 0 \leq k \leq m. \end{aligned} \tag{18}$$

This equation for updating a_k coefficients and the similar one for the b_k coefficients form a coupled system of equations, where within a cell, the unknowns for all modes are coupled. Therefore, inversion of the Left-Hand-Side (LHS) implicit matrix would be computationally costly, especially when a high number of modes are included. A similar approach as the one used for the decoupling of the neighboring cell effects, by employing an iterative Gauss-Seidel approach in the spatial direction, can be used to decouple the modes. Therefore, using this approach in the temporal direction enables all modes, where $\gamma \neq k$, to be transferred to the RHS. Therefore, the coupling effects of the modes are treated as source terms which are updaded within a sub-sub-iteration over the modes. As a result, for the resulted segregated system of equations, on the LHS, only the desired coefficient of one mode remains, while on the RHS, the remaining modes and cells are included,

$$\begin{aligned}\left[\frac{1}{\Delta t^*}+\frac{\partial a'_k}{\partial a_k}\right](a_k^{n+1,s+1,g+1}-a_k^{n+1,s+1,g}) = -\Bigg\{\frac{a_k^{n+1,s+1,g}-a_k^n}{\Delta t^*}+\frac{2\pi k}{T}b_k^{n+1,s+1,g} \\ +a'^{n+1,s}_k+\sum_{\gamma=0}^{m}\frac{\partial a'_k}{\partial a_\gamma}(a_\gamma^{n+1,s+1,g}-a_\gamma^{n+1,s})+\sum_{\gamma=1}^{m}\frac{\partial a'_k}{\partial b_\gamma}(b_\gamma^{n+1,s+1,g}-b_\gamma^{n+1,s})\Bigg\} \quad \forall \quad 0\le k\le m.\end{aligned} \tag{19}$$

The equations for the a_k coefficients are coupled on the RHS with the equations for the b_k coefficients through the source terms (terms including $\frac{2\pi k}{T}$) and the terms in the summation signs.

As it is observed, in this method, three sets of iterations within the n, s and g loops should be performed. Iteration within the n-loop is introduced to ensure the nonlinear dependence of $\hat{R}$ to $\hat{w}$. The sub-iteration within the s-loop is employed to transfer the contribution of the neighboring cells in the spatial discretization of the fluxes to the RHS. Finally, the sub-sub-iterations within the g-loop enable us to update the unknowns of each mode separately, while the coupling effects of the other modes are transferred to the RHS.

The four by four LHS matrix in Eq. (19) is stored in a factorized LU form for all of the modes at each cell. Since the time marching within the n-loop is in pseudo time, a high level of convergence both in the s and g loops is not necessary and 3 to 10 iterations are sufficient for these inner loops.

2.3 Adaptive NLFD Implementation

2.3.1 Fourier Series Augmentation

The need for a high number of modes for highly unsteady flows restricts the usage of the NLFD method due to the computational memory and efficiency limitations. This problem could be reduced if within each individual computational cell, the Fourier series representing the flow solution are adaptively augmented, in such a way that higher number of modes are introduced in regions of the flow, where larger amount of unsteadiness is present. In the frequency analysis, the contribution of each mode in the solution is through the coefficient of that mode (a_k and b_k or $\hat{w}_k$ in Eq. (7)). These coefficients could be averaged and non-dimensionalized to form a single number known as the Spectral Energy (SE). For each mode, the spectral energy is defined as,

$$\mathrm{SE}_k = \frac{|\hat{w}_k|}{\sum_{k=0}^{m}|\hat{w}_k|}, \tag{20}$$

where

$$|\hat{w}_k| = \sqrt{\Re\{\hat{w}_k\}^2+\Im\{\hat{w}_k\}^2} = \sqrt{\hat{w}_k\hat{w}_{-k}} = \sqrt{\hat{w}_k\bar{\hat{w}}_k}. \tag{21}$$

To set a criteria for the Fourier series augmentation, at each control volume, the spectral energy of the last mode is compared with a Reference Spectral Energy (RSE). The reference spectral energy is a user threshold to maintain a minimum desired level of spectral energy in the highest mode. Through the adaptation procedure, initially only one mode is assigned to all of the cells. As the solution progresses, an additional mode is added to each cell if the spectral energy of the highest mode of that cell is above the reference spectral energy. Besides, for the developed adaptation procedure, the possibility of mode reduction is considered as well. This ability is important since during the flow development some of the cells may initially require higher number of modes, but the need seizes once the dominant features of the flow are established. To eliminate the last mode, the spectral energy of the second last mode is compared to the reference spectral energy; if lower, then the last mode is removed.

2.3.2 Flux Adjustment at Temporal-Mismatched Cell Faces

The Fourier series augmentation procedure results into a situation, where two neighboring cells may have different number of modes. Therefore, due to a mismatched in the time instances of the sampled state vectors, special treatments should be done for the flux evaluations across their corresponding interfaces. The time adjustment could be obtained in the time domain by temporary adding or dropping the last mode in the frequency domain and redistributing the samples time instances using an inverse FFT.

3 Results and discussion

For the validation of the developed solver, three physical cases are investigated. Laminar vortex shedding behind (i) a stationary 2D cylinder, (ii) a plunging, and (iii) a pitching airfoil. These cases are chosen to illustrate the capability of the solver for handling the stationary, rigid, and deformable grid movements, respectively.

Depending on the vortex mechanism, periodic vortex shedding behind bluff bodies is categorized into two groups, (i) natural vortex shedding and (ii) induced vortex shedding. In the natural vortex shedding, the periodic behavior is due to the instabilities within the shear layer after the separation of the boundary layer, while for the induced one, moving or oscillating objects are the source of instabilities. Vortex shedding behind stationary bluff bodies belongs to the first group. For these problems, the shedding frequency is not known a prior, while for the induced periodic problems, the shedding frequency is the same as the frequency of the oscillating object.

3.1 Stationary Cylinder

Laminar vortex shedding behind 2D circular cylinders has been extensively investigated both experimentally [25–28] and numerically [17, 29–31]. For this case, laminar von Karman vortex shedding appears in the range of $49 \leq Re \leq 189$, where above $Re \approx 189$, three-dimensional shedding modes are observed, while below $Re \approx 49$ the wake is stationary. In our simulation, $Re = 180$ is chosen, while the Mach number is set to 0.2 to minimize the compressibility effects. Based on an intensive grid study, an o-gird with 256×128 points, in the circumferential and radial directions respectively, is chosen for the simulation.

As it was mentioned, for the laminar vortex shedding behind a stationary cylinder, the shedding frequency is unknown and should be obtained as part of the solution. For the NLFD method, McMullen suggested an optimization-based method for evaluation of this natural frequency. In this study, the same method is used for the cylinder case. Details of this method could be found in McMullen's thesis [15].

Based on a high-order finite element simulation, Henderson [30] proposed four correlations for the Strouhal number, St, base suction coefficient, $-C_{pb}$, pressure drag coefficient, C_{Dp}, and skin friction drag coefficient, C_{Df}, which are widely used as universal benchmarks by other researchers [29, 32–34].

$$\begin{aligned}
St &= a_0 - a_1 Re^{a_2} \exp(a_3 Re), \\
C_{Df} &= a_0 / Re^{a_1}, \\
C_{Dp} &= a_0 - a_1 Re^{a_2} \exp(a_3 Re), \\
-C_{pb} &= a_0 - a_1 Re^{a_2} \exp(a_3 Re).
\end{aligned} \tag{22}$$

The required coefficients for these correlations are presented in Table 1. These correlations are used for validation of our numerical simulation.

Table 1: Coefficients of Henderson [30] universal curves.

	a_0	a_1	a_2	a_3
St	0.2417	0.8328	-0.4808	-1.895×10^{-3}
$-C_{pb}$	1.7826	1.6575	-0.0427	-2.66×10^{-3}
C_{Dp}	1.4114	0.2668	0.1648	-3.375×10^{-3}
C_{Df}	2.5818	0.4369	-	-

To illustrate the computational improvement that is achieved from the adaptive NLFD method over the non-adaptive approach, a thorough temporal analysis is demonstrated. For the NLFD method, the number of modes are fixed and predetermined; therefore, for the temporal accuracy study, different number of modes should be tried to achieve a desired level of accuracy for the mentioned flow coefficients. Table 2 shows that, in order to have all coefficients accurate up to the fourth decimal place, the NLFD method with $m = 6$ modes is required. On the other hand, for the adaptive NLFD method, instead of a fixed number of modes, the reference spectral energy is used to satisfy a desired level of temporal accuracy for the solution. For instance, to have the same accurate results as the NLFD method, the reference spectral energy should be set to RSE $\lesssim 10^{-5}$. This value ensures that the error of the temporal discretization in the flow solution is at the fifth decimal place, while the digits up to the fourth decimal place are accurately converged. The desired flow coefficients obtained from the adaptive NLFD method with RSE $= 10^{-5}$ is presented in the last row of table 2. The table shows that although just a fraction of cells, 6.5%, have 6 modes in their Fourier representations for the adaptive approach, the desired flow coefficients are identical to those of the NLFD method with $m = 6$.

In figure 1, the L_2 norm convergence for each mode of the total residual, $\hat{R}^*_k$, is presented for the adaptive NLFD method. It is observed that all of the modes converge to machine zero with almost similar rates. If the time period correction algorithm was not used, this level of convergence would not be obtained. In this figure, region (I) represents a two-order convergence of the NLFD scheme with a single mode. This ensures that the average flow components have converged to a reasonable starting solution for the adaptive NLFD method. In region (II), the modes are adapted, while in region (III) cells are no longer adapted, allowing the residuals to accelerate to machine zero convergence. It should be noted that the adaptation and reconstruction of the fluxes across mismatched cell faces does not compromise the stability of the flow solver. A machine zero convergence is achieved for all cases presented in this study.

In figure 2, the vorticity distribution contours for the employed adaptive (figure 2(a)) and non-adaptive NLFD method with $m = 6$ (figure 2(c)) is presented. Comparing these vorticity contours demonstrates that similar to the flow coefficients (table 2), identical field-distributed contours are achieved through using the adaptive concept. The modal distribution of the adaptive method is presented in figure 2(b). The figure shows that one up to six modes are assigned to the cells depending on the local level of unsteadiness, where a higher number of modes are required for the cells within the wake and lower modes represents the flow solution in the upstream region. For more validation of the adaptive approach, a post-processed modal

Table 2: Temporal study for the 2D laminar vortex shedding behind a stationary cylinder at $Re = 180$.

Method	Number of Modes	St	$-\bar{C}_{pb}$	$\bar{C}_{Dp}$	$\bar{C}_{Df}$	$\bar{C}_{Dt}$
NLFD	1	0.1755	0.8322	1.0134	0.2513	1.2647
	2	0.1923	0.9077	1.0644	0.2606	1.3250
	3	0.1875	0.9214	1.0696	0.2612	1.3308
	4	0.1881	0.9287	1.0743	0.2621	1.3363
	5	0.1883	0.9293	1.0748	0.2622	1.3370
	6	0.1882	0.9297	1.0751	0.2622	1.3373
adaptive NLFD	1-6	0.1882	0.9297	1.0751	0.2622	1.3373

distribution for the non-adaptive NLFD approach is presented in figure 2(d). To obtain this contour for the NLFD method, within each cell, the spectral energy of each mode is evaluated and compared with a reference spectral energy (similar to the value used for the adaptive approach (RSE $= 10^{-5}$)), if lower, the remaining modes are removed. Comparing this post-processed modal distribution for the NLFD method (figure 2(d)) with the obtained modal distribution during the adaptive approach (figure 2(b)) emphasizes the accuracy of the adaptive approach.

In figure 3(a), instantaneous total lift coefficients over a time period for the adaptive and non-adaptive NLFD methods are presented. From the figure, it is observed that the solution converges as the number of modes for the NLFD method is increased, while the adaptive approach compares extremely well. In figure 3(b), the total drag and base suction coefficients of the adaptive approach are compared to the numerical results of Gopinath and Jameson [17]. The figure demonstrates that both solutions exhibit similar time periods and peak values for the respective curves.

In order to quantitatively illustrate the achieved computational efficiency which is obtained through using the adaptive over the non-adaptive approach, the L_2 norm convergence rates of the mean flow components of the NLFD with $m = 6$ and the adaptive NLFD method with RSE $= 1^{-5}$ are compared. The results are presented in figure 4(a) and show a speed up of $\alpha \approx 1.7$ by using the adaptive approach. Comparing the memory usage factor of these two approaches reveals that through the adaptive method only 56% of the needed memory by the non-adaptive method is required. Memory usage factor is proportional to the Degrees of Freedom (DoF) of a problem which could be evaluated by computing the total number of time instances which the flow solution should be kept.

A great computational improvement is achieved by using the developed implicit temporal discretization over an explicit one. For the comparison, a modified five-stage Runge-kutta scheme, which is a popular explicit approach is used [13, 14, 35, 36]. The results are presented in figure 4(b) and show a speed-up factor of 21 to achieve machine-zero accuracy. In fact, the time step limitation for the explicit approaches results into a large number of pseudo iterations, while for the developed implicit approach, there is no stability criteria for the selected marching time step. Since the temporal accuracy of the results is a function of number of employed modes, not the pseudo time step, the results of the explicit and implicit methods are identical up to the desired fourth decimal place.

3.2 Plunging Airfoil

In this section, the laminar vortex shedding behind a vertically plunging NACA0012 airfoil is investigated. The plunging motion of the airfoil is expressed as $y(t) = h\sin(\omega t)$, where h is the plunging amplitude and $\omega = 2\pi f$ is the plunge circular frequency. For this case, the non-dimensionalized plunging frequency, Strouhal number ($St = \dfrac{\omega hc}{V_\infty} = 0.46$) is used. Besides, similar to the cylinder case, $M = 0.2$ is used to minimize the compressibility effects. As for the plunging amplitude, $\dfrac{h}{c} = 0.08$ is employed where the grid rigidly and vertically oscillates. A C-grid topology is used for the grid with 256×128 cells based on an intensive grid study. For the selected grid, the first cell spacing is 10^{-4} and the farfield distance is 15 chord lengths. Again, to acquire fourth-decimal-place temporal accuracy, the reference spectral energy is set to 10^{-5} for the adaptive NLFD approach. This case is experimentally investigated by Jones *et.* al. [37], while Jameson and Liang [38] numerically simulate the problem using a spatially high-order spectral difference approach.

In figure 5, the experimentally visualized streak lines of the flow obtained by Jones *et.* al. [37] (figure 5(a)), vorticity contours numerically obtained by Jameson and Liang [38] with a 3^{rd} order spatial discretization (figure 5(b)), and vorticity contours of the present study using the adaptive NLFD approach (figure 5(c)) are presented. Comparing these contours qualitatively validates our simulation. In figure 5(d) the resulted modal distribution is presented for our adaptive NLFD simulation. The figure shows that, if a fourth-decimal-place order of accuracy is desired for the results, a maximum of 13 modes should be assigned to the cells within the wake, where the vortices shed behind the airfoil.

Table 3: The flow coefficients for the simulated pitching airfoil.

	$\bar{C}_{Df}$	$\bar{C}_{Dp}$	$\bar{C}_{Dt}$	$\hat{C}_{Lt}$
adaptive NLFD	0.0859	0.0280	0.1139	0.7231
Pedro *et* al. [39]	0.0857	0.0276	0.1132	0.7107

The instantaneous lift and drag coefficients over a period for the plunging airfoil case are presented in figure 6. The numerical results of Jameson and Liang [38] are super imposed on the curves as well. A very good agreement is achieved between the results, although a 4^{th} order spacial discretization scheme is used by Jameson and Liang [38].

3.3 Pitching Airfoil

To illustrate the capability of the developed deformable grid concept, a pitching NACA0012 airfoil is numerically investigated. The pitching motion follows $\theta = \theta_{\text{max}} \sin(\omega t)$, where the maximum pitching angle is $\theta_{\text{max}} = 5°$. The pitching reduced frequency is $\kappa = \dfrac{\omega c}{2V_\infty} = 2$, and again, Mach number is set to 0.2. The flow Reynolds number is 1100. This test case is numerically investigated by Pedro *et* al. [39], where a second-order finite volume method was employed for the numerical simulation of a flapping hydrofoil.

For the base grid, the same grid as the one used for the plunging aifoil is employed, while the pitching motion is performed through the deformation of the grid. In figure 7, three instantaneous snapshots of the grid are presented, where the angle of attack is $\theta = 0°$ (figure 7(a)), $\theta = \theta_{\text{max}} = 5°$ (figure 7(b)), and $\theta = \theta_{\text{min}} = -5°$ (figure 7(c)). The figures show how the grid points are perturbed over the airfoil surface to handle these deformations, while the cells along the trailing edge remain fix. In order to preserve the airfoil shape through the rotation in the time domain, 4 modes are considered in the Fourier representation of the grid in the frequency domain. This means that 9 initial snapshots of the grid is needed in the time domain sampled at evenly distributed intervals over the time period. Therefore, the grids are generated for the airfoil at $\theta = (40m)°$, where m is valued from 0 to 8. This is unlike the time marching approaches, which the grid should either be perturbed or reproduced after each time step. In this study, for the required angle of attacks, a hyperbolic grid generator method is used.

For this case, the vorticity and modal distribution contours are presented in figure 8(a) and 8(b), respectively. The instantaneous lift and drag coefficients over a period is presented in figure 9, while in table 3, the time-averaged friction, pressure, and total drag coefficients as well as the maximum lift coefficient of the present study are compared with those of Pedro *et* al. [39].

References

[1] JOSEPH M. Verdon and JOSEPH R.Caspar. A linearized unsteady aerodynamic analysis for transonic cascades. *Journal of Fluid Mechanics*, 149:403–429, 1984.

[2] Joseph M. Verdon and Joseph R. Caspar. Subsonic flow past an oscillating cascade with finite mean flow deflection. *AIAA JOURNAL*, 18(5):540–548, 1980.

[3] F. Edward Ehlers and Warren H. Weatherill. A harmonic analysis method unsteady transonic flow its application flutter airfoils. Contractor Report 3537, NASA, May 1982.

[4] K. C. Hall and E. F. Crawley. A linearized Euler analysis of unsteady flows in turbomachinery. Technical report, June 1987.

[5] Kenneth C. Hall and Edward F. Crawley. Calculation of unsteady flows in turbomachinery using the linearized euler equations. *AIAA Journal*, 27(6):777–787, June 1989.

[6] W.S. Clark and K.C. Hall. A time-linearized navier-stokes analysis of stall flutter. *Journal of Turbomachinery*, 122(3):467–476, 2000.

[7] J. J. Adamczyk. Model equation for simulating flows in multistage turbomachinery. Technical report, NASA Technical Memorandum 86869., Nov 1984.

[8] W. Ning and L. He. Computation of unsteady flows areound oscillating blades using linear and nonlinear harmonic euler methods. *Journal of Turbomachinery*, 120:508–514, July 1998.

[9] L. He and W. Ning. Efficient approach for analysis of unsteady viscous flows in turbomachines. *AIAA Jornal*, 36(11):2005–2012, November 1998.

[10] K. C. Hall. Seminar on harmonic balance techniques. Technical report, Presented to the Aerospace Computing Lab, Stanford University, 2000.

[11] K. C. Hall, J. P. Thomas, and W. S. Clark. Computation of unsteady nonlinear flows in cascades using a harmonic balance technique. Technical report, 9th International Symposium on Unsteady Aerodynamics, Aeroacoustics and Aeroelasticity of Turbomachines, Lyon, France, September 2000.

[12] K.C. Hall, J.P. Thomas, and W.S. Clark. Computation of unsteady nonlinear flows in cascades using a harmonic balance technique. *AIAA Journal*, 40, 2002.

[13] Matthew McMullen, Antony Jameson, and Juan Alonso. Demonstration of nonlinear frequency domain methods. *AIAA Journal*, 44, No. 7:1428–1435, 2006.

[14] M. McMullen and A. Jameson. The computational efficiency of non-linear frequency domain methods. *Journal of Computational Physics*, 212:637–661, 2006.

[15] Matthew McMullen. *The Application of Non-Linear Frequency Domain Methods to the Euler and Navier-Stokes Equations*. Ph.d. dissertation, Department of Aeronautics and Astronautics, Stanford University, Stanford, CA, March 2003.

[16] M. McMullen, A. Jameson, and J. Alonso. Acceleration of convergence to a periodic steady state in turbomachinery flows. AIAA Paper 01-0152, 39th. Aerospace Sciences Meething and Exhibit, Reno, NV, Jan 2001.

[17] A. Gopinath and A. Jamesonn. Application of the time spectral method to periodic unsteady vortex shedding. Aiaa paper, 44^{th} Aerospace Meeting and Exhibit, January 2006.

[18] Raymond C. Maple, Paul I. King, and Mark E. Oxley. Adaptive harmonic balance solutions to euler's equation. *AIAA Journal*, 41 No. 9:1705–1714, 2003.

[19] Ali Mosahebi Mohamadi and Siva K. Nadarajah. An adaptive non-linear frequency domain method for viscous periodic steady state flows. Technical report, 48th AIAA Computational Fluid Dynamics Conference, January 2010.

[20] J-S. Cagnone and S. K. Nadarajah. Implicit nonlinear frequency-domain spectral-difference scheme for periodic euler flow. *AIAA Journal*, 47, No. 2:361–372, 2009.

[21] Ali Mosahebi and Siva K. Nadarajah. An implicit adaptive nonlinear frequency domain method (pnlfd) for viscous periodic steady state flows on deformable grids. Technical report, 49th AIAA Computational Fluid Dynamics Conference, January 2011.

[22] P.L Roe. Approximate riemann solvers, parameter vectors, and difference schemes. *Journal of Computational Physics*, 43(2):357 – 372, 1981.

[23] Bram van Leer. Towards the ultimate conservative difference scheme. v. a second-order sequel to godunov's method. *Journal of Computational Physics*, 32(1):101 – 136, 1979.

[24] J. Blazek. *Computational Fluid Dynamics:Principles and Applications*. ELSEVIER, 2001.

[25] C.H.K. Williamson and G.L. Brown. A series in (1/sqrt(re)) to represent the strouhal-reynolds number relationship of the cylinder wake. *J. Fluids and Struc.*, 12:1073–1085, 1998.

[26] C.H.K. Williamson. Oblique and parallel modes of vortex shedding in the wake of a circular cylinder at low reynolds numbers. *J. Fluid Mech.*, 206:579–627, 1989.

[27] Williamson. Vortex dynamics in the cylinder wake. *Annual Review of Fluid Mechanics*, 28:477–539, 1996.

[28] C.H.K. Williamson. Defining a universal and continuous strouhal-reynolds number relationship for the laminar vortex shedding of a circular cylinder. *Phys. Fluids*, 31:2742, 1988.

[29] J. Park, K. Kwon, and H. Choi. Numerical solutions of flow past a circular cylinder at reynolds numbers up to 160. *KSME International Journal*, 12 No. 6:1200–1205, 1998.

[30] Ronald D. Henderson. Details of drag curve near the onset of vortex shedding. *Phys. Fluids*, 7:2102–2104, 1995.

[31] A Belov, L Martinelli, and A Jameson. A new implicit algorithm with multigrid for unsteady incompressible flow calculations. AIAA Paper 95-0049, 33rd Aerospace Meeting and Exhibit, January 2005.

[32] A.L.F. Lima E Silva, A. Silveira-Neto, and J.J.R. Damasceno. Numerical simulation of two-dimensional flows over a circular cylinder using the immersed boundary method. *Journal of Computational Physics*, 189(2):351 – 370, 2003.

[33] Oliver Posdziech and Roger Grundmann. Numerical simulation of the flow around an infinitely long circular cylinder in the transition regime. *Theoretical and Computational Fluid Dynamics*, 15:121–141, 2001. 10.1007/s001620100046.

[34] W Ming-Hsun, W. Chih-Yung, Y. Ruey-Hor, W. Ming-Cheng, and W. An-Bang. Experimental and numerical study of the separation angle for flow around a circular cylinder at low reynolds number. *Journal of Fluid Mechanics*, 515:233–260, 2004.

[35] A. Jamesonn, W. Schmidt, and E. Turkel. Numerical solution of the euler equations by finite volume methods using runge-kutta time-stepping schemes. Aiaa paper, 14^{th} Fluid and Plasma Dynamic Conference, Jun 1981.

[36] S. Nadarajah, M. McMullen, and A. Jameson. Aerodynamic shape optimization for unsteady three-dimensional flows. *International Journal of Computational Fluid Dynamics*, 20(8):533–548, 2006.

[37] K Jones, C. Dohring, and M. Platzer. *AIAA Journal*, 36 No. 7:1240–1246, 1998.

[38] A Jameson and C Liang. Unsteady flow past a plunging airfoil. Workshop on vortex dominated flows, National Institute of Aerospace, June 2009.

[39] G. Pedro, A. Suleman, and N. Djilali. A numerical study of the propulsive eciency of a apping hydrofoil. *INTERNATIONAL JOURNAL FOR NUMERICAL METHODS IN FLUIDS*, 42:493–526, 2003.

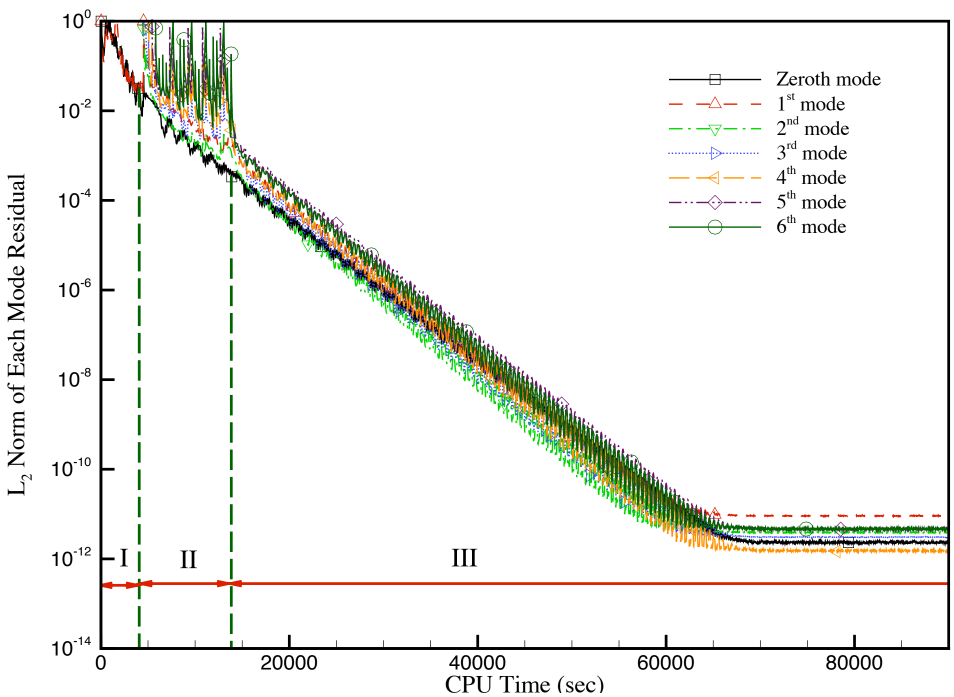

Figure 1: Convergence of the L_2 norm for all of the modes of the residual, $\hat{R}_k^*$ for the adaptive NLFD method.

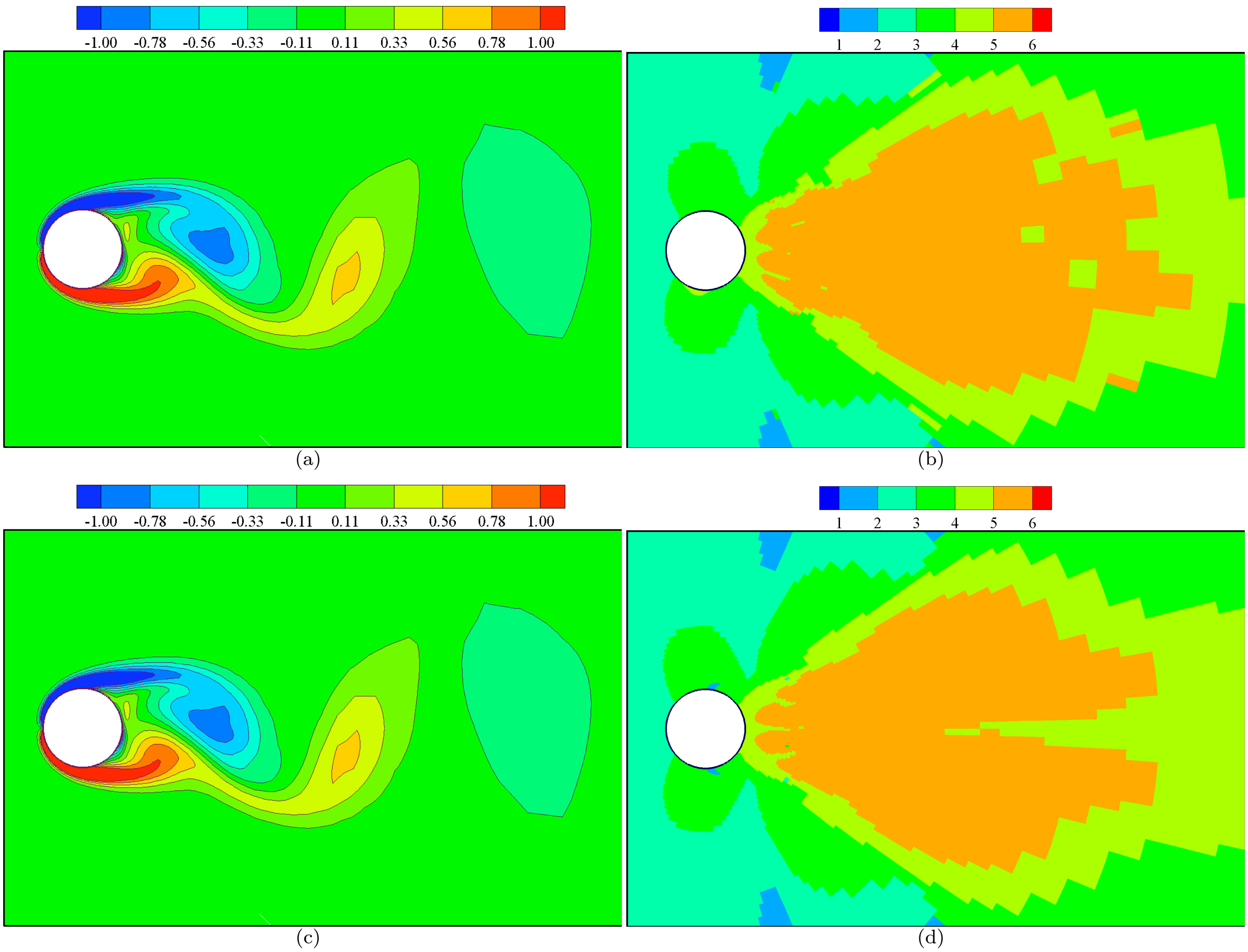

Figure 2: Laminar vortex shedding behind a 2D cylinder at $Re = 180$: adaptive NLFD method with RSE $= 10^{-5}$ (a) vorticity contour, (b) modal distribution ; NLFD method with $m = 6$ modes (c) vorticity contour, (d) post-processed modal distribution using RSE $= 10^{-5}$.

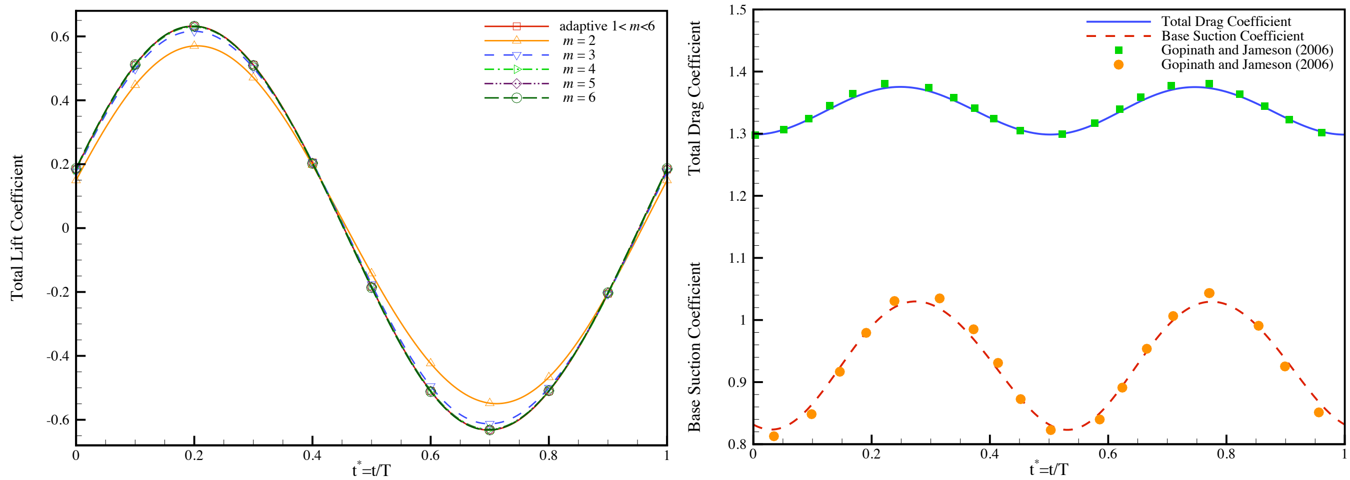

(a) (b)

Figure 3: Laminar vortex shedding behind a 2D cylinder at $Re = 180$: (a) total lift versus the non-dimensional time over one period for the NLFD method with $m = 2$ up to $m = 6$ modes and the adaptive NLFD method with RSE $= 1^{-5}$, (b) comparison of the total drag and base suction coefficients of the adaptive NLFD method with the numerical results of Gopinath and Jameson [17].

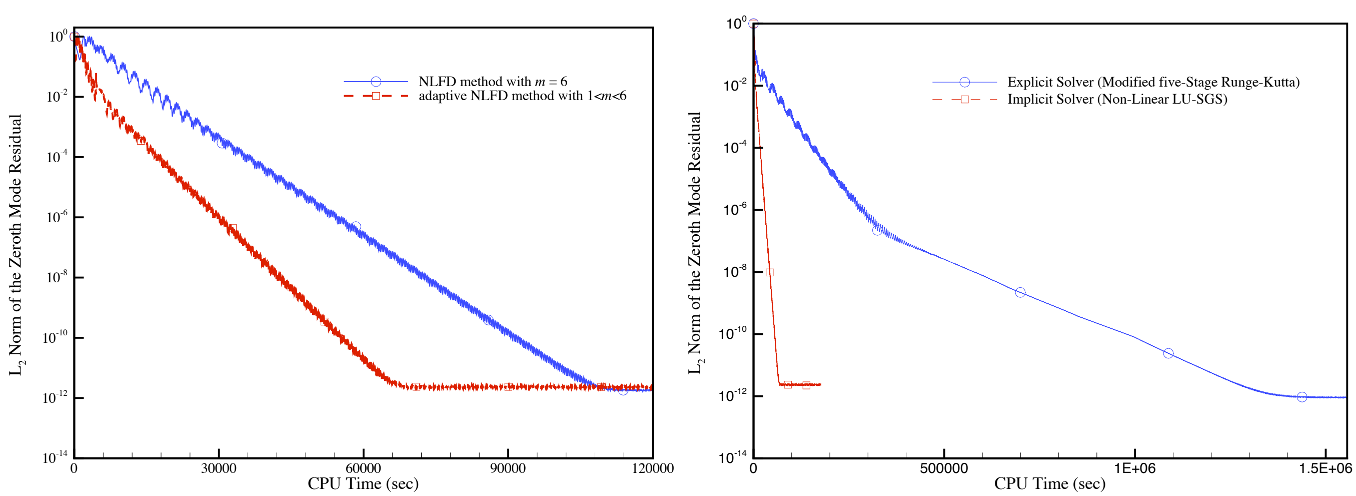

(a) (b)

Figure 4: Convergence of the L_2 norm for the zeroth mode of the residual, $\hat{R}_0^*$; (a) adaptive versus non-adaptive NLFD method, (b) implicit versus explicit temporal discretization.

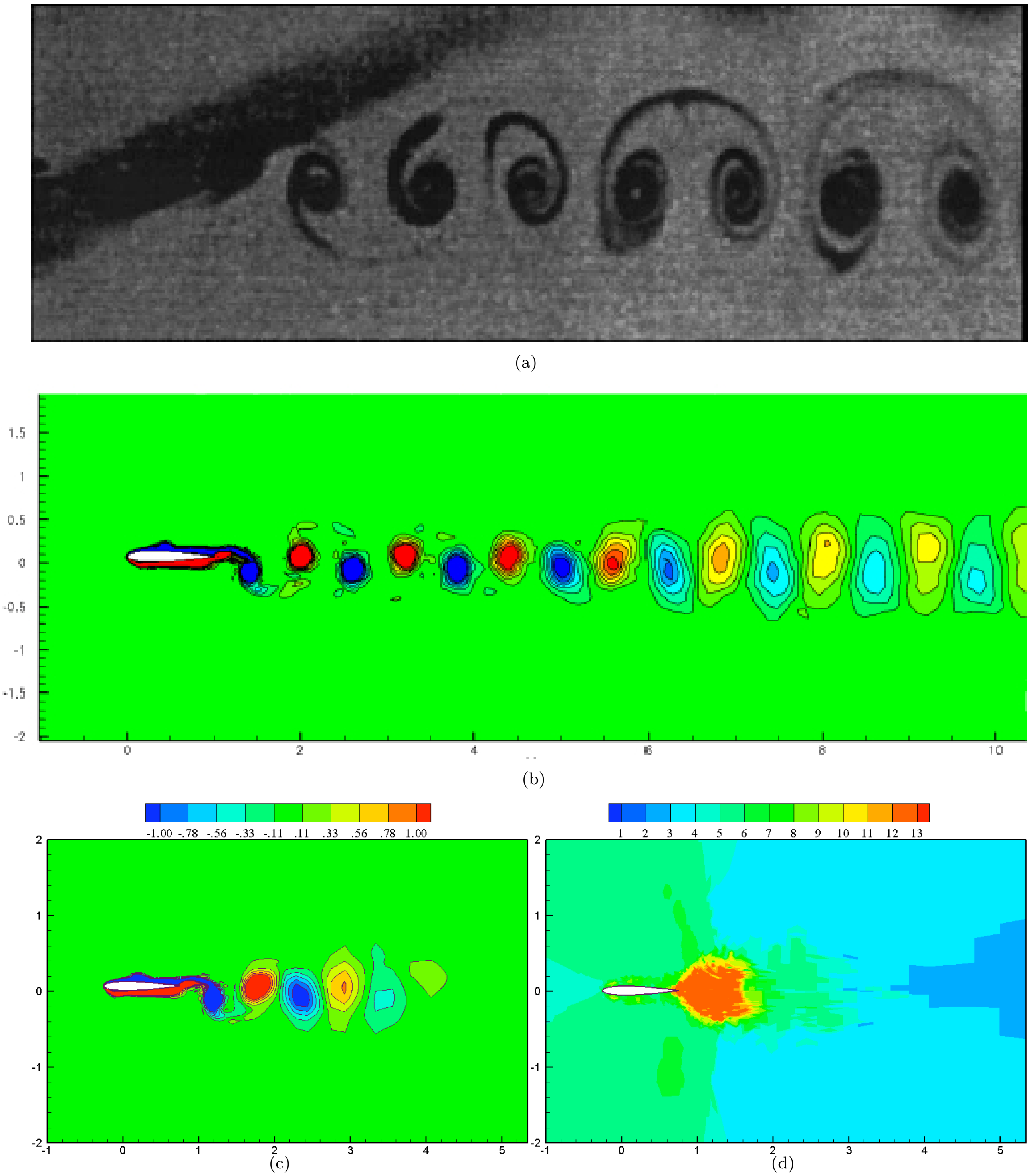

Figure 5: Laminar vortex shedding behind the plunging airfoil with $h = 0.08$, $St = 0.46$, and $Re = 1850$ using adaptive NLFD method with $\mathrm{RSE} = 10^{-5}$: (a) visualized streak lines from the experimental results of Jones *et.* all. [37], (b) vorticity contour from numerical results of Jameson and Liang [38] using a 3^{rd} order spatial discretization scheme, (c) vorticity contour of the present study, and (d) modal distribution of the present study.

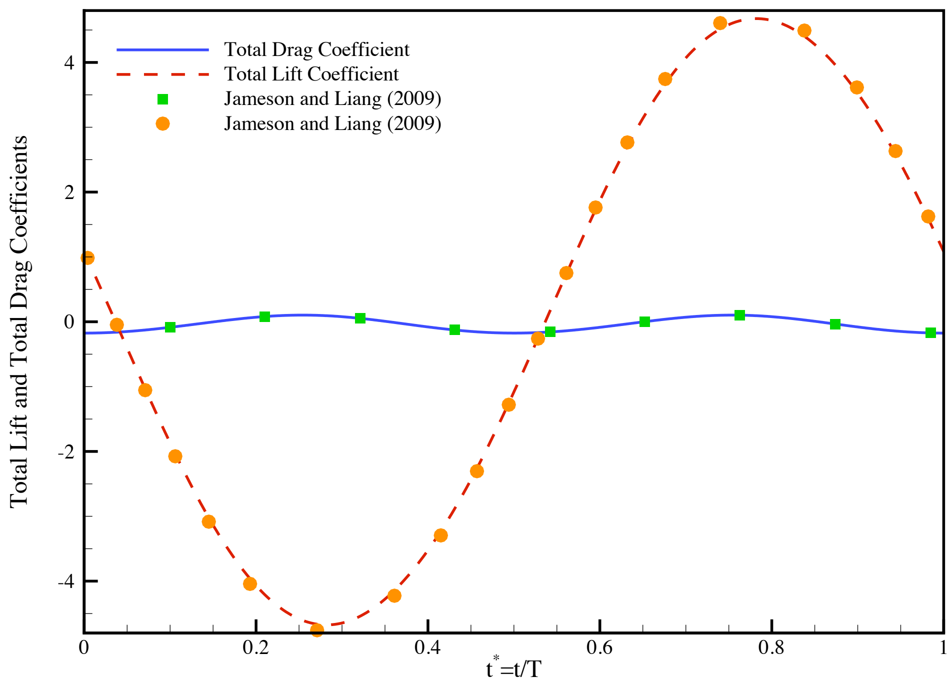

Figure 6: Instantaneous total lift and drag coefficients over a non-dimensionalized time period for the plunging airfoil with $h = 0.08$, $St = 0.46$, and $Re = 1850$ using adaptive NLFD method with RSE $= 10^{-5}$. The obtained results are compared with those of Jameson and Liang [38] using a 4^{rd} order spatial discretization scheme.

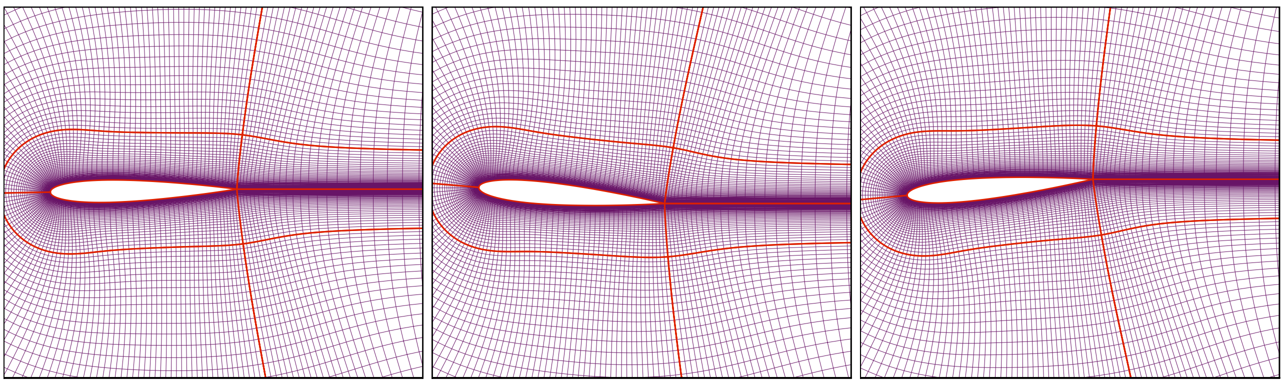

(a) (b) (c)

Figure 7: Instantaneous snapshots of the grid at 3 time instances (a) angle of attack is $\theta = 0$, (b) $\theta = \theta_{\max} = 5°$, and (c) $\theta = \theta_{\min} = -5°$.

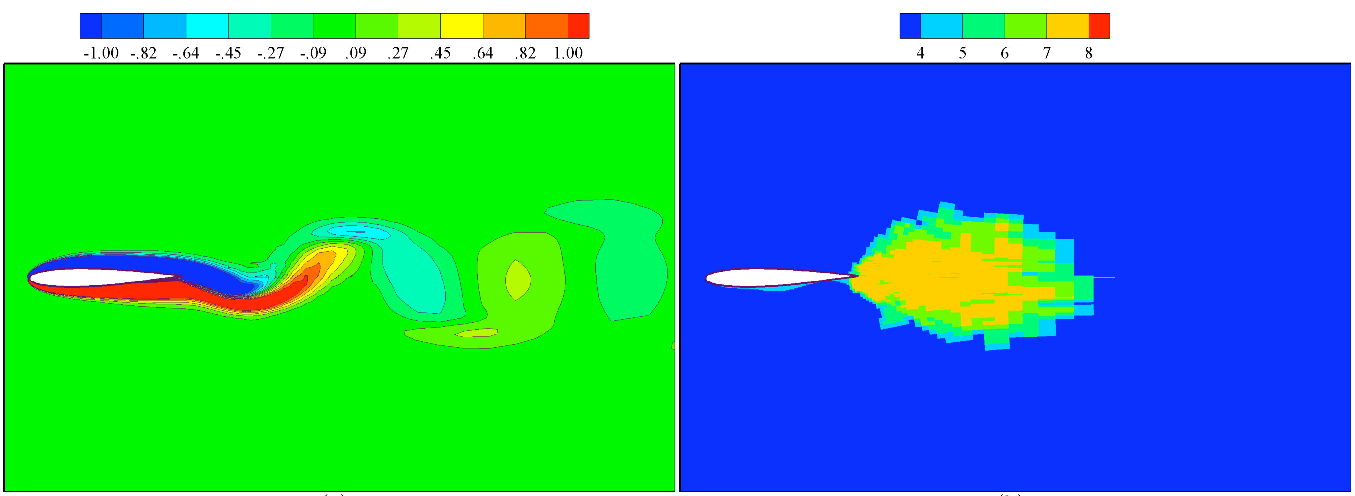

(a) (b)

Figure 8: Laminar vortex shedding behind a pitching airfoil with $\theta_{\max} = 5°$, $\kappa = 2$, and $Re = 1100$ using adaptive NLFD method with RSE $= 10^{-5}$ (a) vorticity contour and (b) modal distribution.

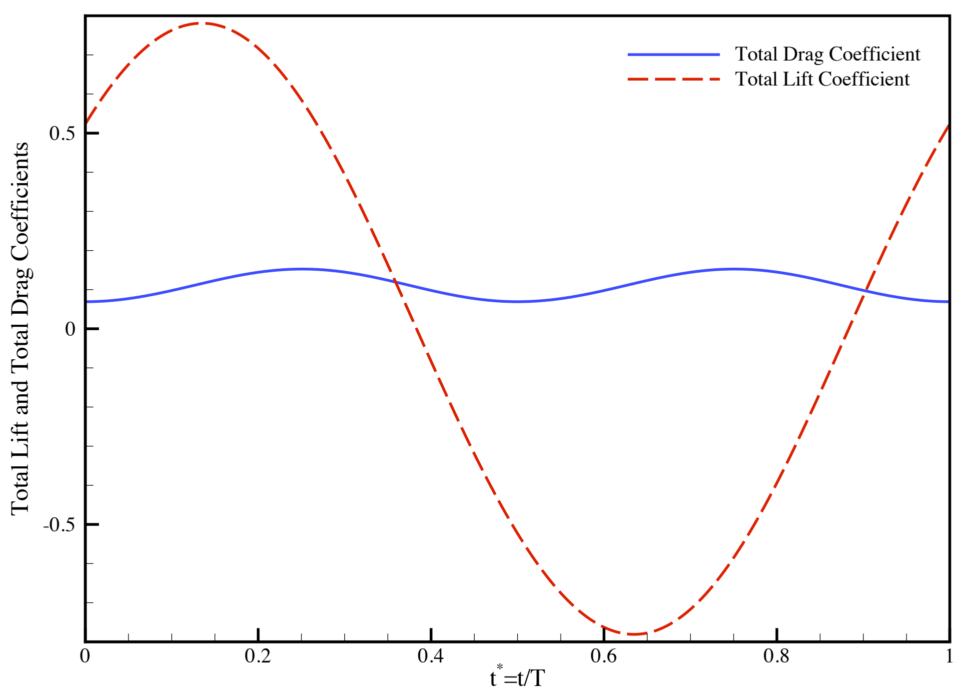

Figure 9: Instantaneous total lift and drag coefficients over a non-dimensionalized time period for the pitching airfoil with $\theta_{\max} = 5^\circ$, $\kappa = 2$, and $Re = 1100$ using adaptive NLFD method with RSE $= 10^{-5}$